Improving the Stability of Non-Noble-Metal M–N–C Catalysts for Proton-Exchange-Membrane Fuel Cells through M–N Bond Length and Coordination Regulation

Zhengpei Miao, Xiaoming Wang, Zhonglong Zhao, Wenbin Zuo, Shaoqing Chen, Zhiqiang Li, Yanghua He, Jiashun Liang, Feng Ma, Hsing-Lin Wang, Gang Lu, Yunhui Huang, Gang Wu, and Qing Li*

An effective and universal strategy is developed to enhance the stability of the non-noble-metal M–N_x/C catalyst in proton exchange membrane fuel cells (PEMFCs) by improving the bonding strength between metal ions and chelating polymers, i.e., poly(acrylic acid) (PAA) homopolymer and poly(acrylic acid–maleic acid) (P(AA-MA)) copolymer with different AA/MA ratios. Mössbauer spectroscopy and X-ray absorption spectroscopy (XAS) reveal that the optimal P(AA-MA)–Fe–N catalyst with a higher Fe^{3+}–polymer binding constant possesses longer Fe—N bonds and exclusive Fe–N_4/C moiety compared to PAA–Fe–N, which consists of ≈15% low-coordinated Fe–N_2/N_3 structures. The optimized P(AA-MA)–Fe–N catalyst exhibits outstanding ORR activity and stability in both half-cell and PEMFC cathodes, with the retention rate of current density approaching 100% for the first 37 h at 0.55 V in an H_2–air fuel cell. Density functional theory (DFT) calculations suggest that the Fe–N_4/C site could optimize the difference between the adsorption energy of the Fe atoms on the support (E_{ad}) and the bulk cohesive energy (E_{coh}) relative to Fe–N_2/N_3 moieties, thereby strongly stabilizing Fe centers against demetalation.

Proton-exchange-membrane fuel cells (PEMFCs) are now well-known as promising sustainable electrochemical energy conversion devices, especially for transportation applications.[1] Currently only platinum-group metals (PGMs) can effectively catalyze the kinetically sluggish oxygen reduction reaction (ORR) at the cathode,[2] but the prohibitive cost and geographical scarcity of Pt severely hinder the large-scale implementation of PEMFCs.[3] Therefore, it is extremely desirable to develop PGM-free catalysts to partially or fully replace PGM catalysts.[4] Metal–nitrogen–carbon (M–N–C, M=Fe, Co, Mn, etc.) catalysts with M–N_x/C active sites, especially Fe–N–C catalysts, have exhibited outstanding initial ORR activity in both half-cell and PEMFC testings, rivaling that of the commercial Pt/C catalyst.[4c,e,5] However, numerous and arduous obstacles must be overcome before the M–N–C catalysts can be applied practically in PEMFCs, with stability being the most serious of these challenges.[3c] Specifically, the typical operating conditions of a PEMFC are at 60–80 °C, 0.5–0.8 V, and in strongly acidic and humid environments, where most of the commonly used non-noble metals (Fe, Co, Mn, etc.) are prone to oxidization and being etched away. Although several reported M–N–C catalysts have exhibited decent stability in the acidic electrolyte in half-cell tests at room temperature,

Z. Miao, Z. Li, J. Liang, Dr. F. Ma, Prof. Y. Huang, Prof. Q. Li
State Key Laboratory of Material Processing and Die & Mould Technology
School of Materials Science and Engineering
Huazhong University of Science and Technology
Wuhan, Hubei 430074, China
E-mail: qing_li@hust.edu.cn
Prof. X. Wang
Department of Chemistry and Key Laboratory for Preparation
and Application of Ordered Structural Materials of Guangdong Province
Shantou University
Shantou 515063, China
Dr. Z. Zhao, Prof. G. Lu
Department of Physics and Astronomy
California State University Northridge
Northridge, CA 91330, USA

W. Zuo
Key Laboratory of Artificial Micro
and Nano-Materials of Ministry of Education and Hubei Key Laboratory
of Nuclear Solid Physics
School of Physics and Technology
Wuhan University
Wuhan 430072, China
Dr. S. Chen, Prof. H.-L. Wang
Department of Materials Science and Engineering
Southern University of Science and Technology
Shenzhen, Guangdong 518055, China
Y. He, Prof. G. Wu
Department of Chemical and Biological Engineering
University at Buffalo
The State University of New York
Buffalo, NY 14260, USA

the performance of a PEMFC with M–N–C cathodes typically degrades by >50% in the first 20–50 h of testing (cell voltage > 0.5 V).[1a,4e,6] So far, there are four possible mechanisms to account for the instability of Fe–N–C catalysts in the PEMFCs:[7] 1) the demetalation of Fe–N_x/C active sites;[3c,8] 2) carbon corrosion (electrochemical corrosion at high voltages and/or chemical oxidation by H_2O_2);[9] 3) micropore flooding;[10] 4) protonation of surface N-groups and subsequent anion adsorption.[11] However, the exact degradation mechanisms are still under debate, most likely due to the diversity in local coordination environments of metal centers, carbon structures, and pore distribution of the catalysts reported by different research groups. For instance, the demetalation was proposed to occur at crystalline metal particles rather than Fe–N_x/C moieties,[8a,9e] while Dodelet et al.[8c] observed that the demetalation of Fe–N_x/C active sites was the primary cause for the rapid performance decay in the initial stages. On the other hand, Dodelet et al.[10] considered that micropore flooding was instead the primary reason resulting in significant degradation of the catalytic performance. However, detailed research by Banham et al.[7a] suggested that the observed dramatic loss in activity cannot be solely attributed to micropore flooding. Additionally, Mayrhofer et al.[9e] revealed that CO_2 emission would be occurring only at potentials >0.9 V, whereas Shao et al.[7b] detected the CO_2 formation at 0.3 V in the presence of H_2O_2/radicals. Among the four reasons mentioned above, the demetalation of Fe–N_x/C active sites and carbon corrosion are currently considered as the primary cause of performance degradation.[6] It is worth noting that different degradation mechanisms might be coupled, such as carbon oxidation and the strong adsorption of hydroxyl free radicals will result in the fracture of Fe–N bonds. In turn, the leached Fe ions might react with H_2O_2 to generate oxygen-containing radicals via Fenton reaction and further attack the carbon matrix, ionomer, and proton exchange membrane, which ultimately leads to the catalyst deactivation.[7b] In general, due to the poor

understanding of degradation mechanisms and the complex multi-field (mass/electric/heat) coupling environments of the membrane electrode assembly (MEA), it is still extremely challenging to provide effective solutions to improve the stability of M–N–C catalysts in a PEMFC.[12] Thus, the development of high-performance M–N–C catalysts with significantly enhanced stability is urgent for the commercial applications of PEMFCs.[13]

In this work, we demonstrate that the demetalation of active sites should be a primary reason for the degradation of the M–N–C catalysts and develop an effective strategy to improve the stability of M–N–C catalysts in a PEMFC by tuning the M—N bonds. It is found that the Fe—N bond length and coordination of the Fe–N in the final catalysts can be controlled by tuning the binding constant between Fe ions and the polymer during the synthesis, which is achieved by using poly(acrylic acid) (denoted as PAA) homopolymer or poly(acrylic acid–maleic acid) copolymer (denoted as P(AA-MA)) with different ratios of AA/MA as chelating agents. X-ray absorption spectroscopy (XAS) and ^{57}Fe Mössbauer spectroscopy measurements indicate that the average Fe—N bond length of the optimized P(AA-MA)–Fe–N catalyst (exclusively containing Fe–N_4 moieties) is longer than that of its PAA–Fe–N counterpart (with a substantial portion of Fe–N_2/N_3 moieties). As a result, the optimal P(AA-MA)(5-1)–Fe–N catalyst reveals an unusual ORR activity with a half-wave potential ($E_{1/2}$) of 0.843 V versus reversible hydrogen electrode (RHE) in 0.5 M H_2SO_4 as well as high stability with only a 6 mV $E_{1/2}$ shift after 5000 potential cycles at 60 °C. More importantly, it demonstrates high initial performance with a current density of 1.02 A cm^{-2} at 0.6 V as well as respectable stability (the current density retention rate up to 100% after 37 h constant voltage test at 0.55 V) in PEMFC tests. Our strategy can also be applied to Co–N–C and Mn–N–C systems and provides an effective and universal method to improve the stability of M–N–C PGM-free catalysts for PEMFCs.

The preparation of PAA–Fe–N and P(AA-MA)–Fe–N catalysts is illustrated in **Figure 1**. Acrylic acid (AA), which is the
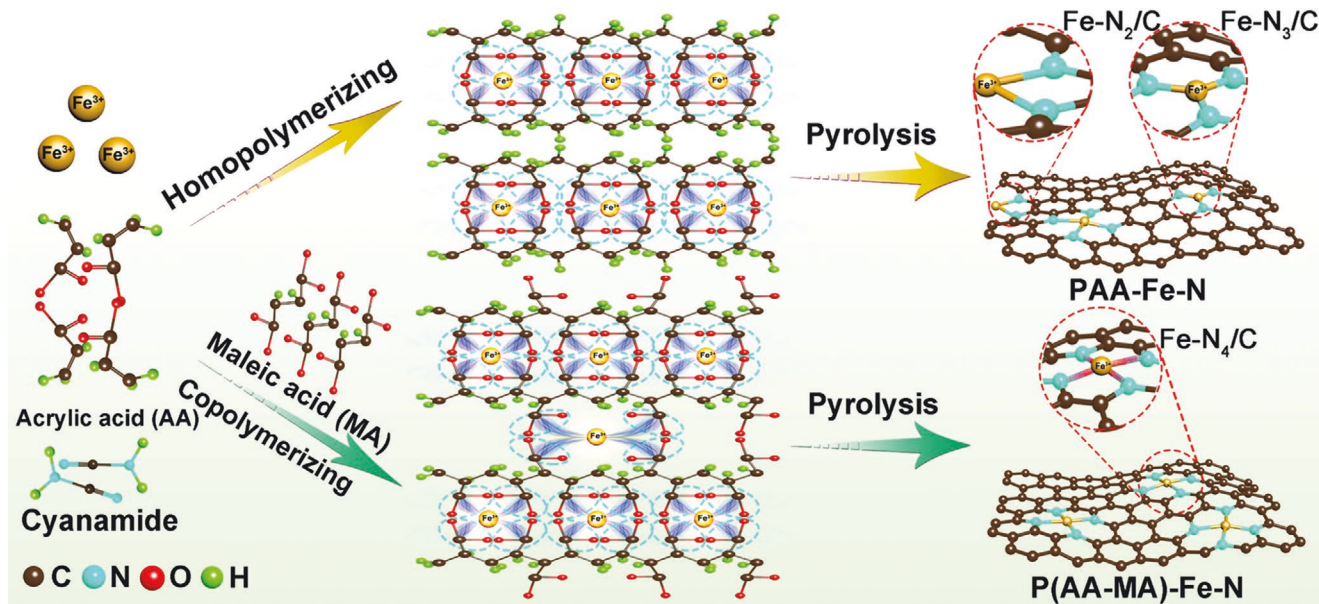

Figure 1. PAA–Fe–N and P(AA-MA)–Fe–N catalysts were prepared by lower binding constant PAA–Fe and higher binding constant P(AA-MA)–Fe as precursor, respectively.

**ADVANCED
SCIENCE NEWS**

www.advancedsciencenews.com

**ADVANCED
MATERIALS**

www.advmat.de

simplest unsaturated monocarboxylic acid, is employed as a monomer to be polymerized into PAA and chelate with Fe^{3+} to form a cross-linked hydrogel.[14] Maleic acid (MA), a dicarboxylic acid monomer, is employed to co-polymerize with AA to increase the carboxylic content of the copolymer (P(AA-MA)) (the chemical structure of the polymers was shown in Figure S1: Supporting Information).[15] By manipulating the molar ratios of AA/MA (5/1, 3/1, 1/1) during copolymerization (denoted as P(AA-MA)(5-1), P(AA-MA)(3-1), P(AA-MA)(1-1), respectively), the concentrations of the carboxylic group in the copolymer and the corresponding binding constant with metal ions can be easily regulated. The cross-linked hydrogel formed by the chelation between hydrophilic carboxylic groups and metal ions can then make the resulting $M-N_x/C$ sites atomically distributed in hierarchical 3D structures through subsequent high-temperature treatment with nitrogen precursors at 800 °C. The resulting catalysts are denoted as PAA–Fe–N and P(AA-MA)–Fe–N, respectively. MA–Fe–N catalyst was also synthesized as a control sample, but MA itself is challenging to polymerize due to the severe steric hindrance of two neighboring carboxylic acid groups.[16]

Isothermal titration calorimetry (ITC) is a powerful microcalorimetric technique used to measure the binding constant (K) and stoichiometry of ligands and metal ions.[17] In this work, the diluted $FeCl_3$ solutions were titrated into the different polymer solutions (PAA, P(AA-MA), etc.) and the binding constants (**Figure 2**a) between Fe^{3+} and polymers can be extracted from the obtained thermograms (Figures S2 and S3: Supporting Information).[18] For P(AA-MA) polymer, there are two sets of binding constants, i.e., K1 and K2, which may corre-

spond to the AA–MA and AA fragments, respectively. Obviously, the binding constant K1 between Fe^{3+} and P(AA-MA) (5-1) (4.5×10^4 M^{-1}) is 18 and 28 times higher than that of PAA and MA, respectively, indicating a much stronger interaction between Fe^{3+} and polymer.

The crystal structures of various P(AA-MA)–Fe–N, PAA–Fe–N, and MA–Fe–N catalysts were investigated by X-ray diffraction (XRD). All of the studied samples exhibit similar diffraction peaks at 24.1° and 43.3°, which can be attributed to the amorphous carbon (Figure 2b). It is worth noting that no Fe-related peaks can be observed in XRD patterns, implying that no visible crystalline Fe species exist in the as-prepared catalysts. Scanning electron microscopy (SEM) (Figures S4 and S5: Supporting Information) and transmission electron microscopy (TEM) images (Figure S6, Supporting Information) of P(AA-MA)–Fe–N and PAA–Fe–N catalysts exhibit distinctively porous and sheet-like structures without any observable Fe-related species. The microstructure of the P(AA-MA)(5-1)–Fe–N catalyst is further imaged by high-angle annular dark-field scanning transmission electron microscopy (HAADF-STEM). The image reveals a uniform dispersion of Fe atoms throughout the carbon matrix, as reflected by bright dots in Figure 2c. Furthermore, the uniform distribution of C, N, O, and Fe elements in the P(AA-MA)(5-1)–Fe–N catalyst is confirmed by elemental mapping through energy-dispersive x-ray spectroscopy (EDX, Figure 2d–i). The specific surface area of various catalysts was measured by nitrogen adsorption/desorption using the Brunauer–Emmett–Teller (BET) method (Figures S7 and S8, Supporting Information). It is obvious that micropores in the catalyst are significantly increased in the presence of MA, which
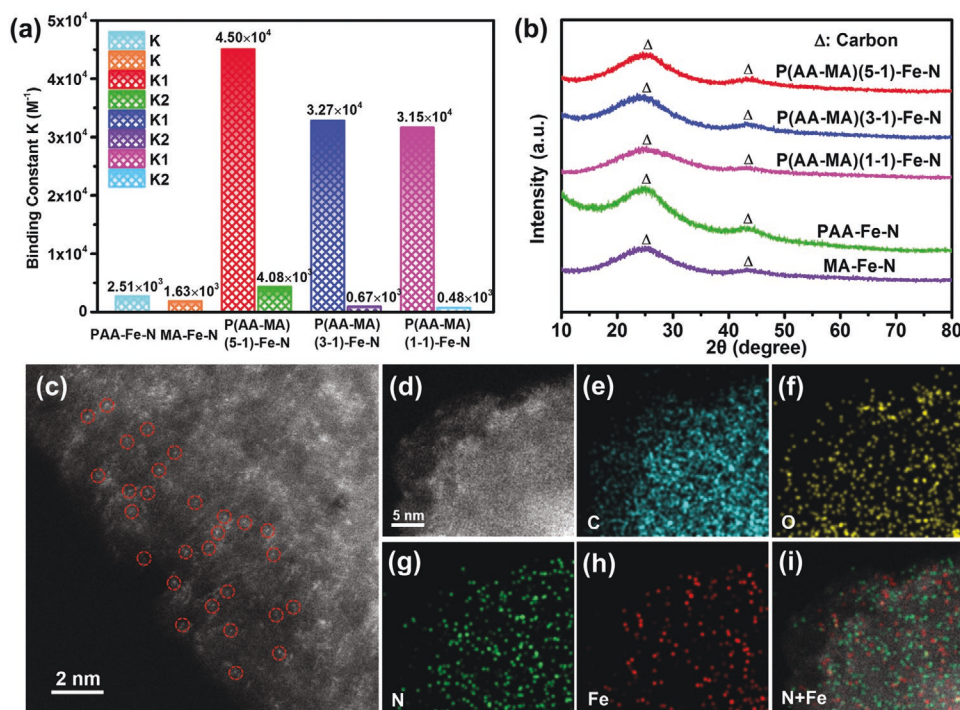

Figure 2. a) The binding constant between Fe^{3+} and the corresponding polymers. b) XRD patterns of various P(AA-MA)–Fe–N, PAA–Fe–N, and MA–Fe–N catalysts. c) HAADF-STEM image (single Fe atoms are highlighted by red cycles), and d–i) HAADF-STEM and the corresponding EDX elemental mapping images of the P(AA-MA)(5-1)–Fe–N sample.

are often viewed as the active site hosts.[7a,19] The abundant micropores for the P(AA-MA)(5-1)–Fe–N catalyst (1088 m² g⁻¹) would benefit a high density of active sites. The Raman spectra (Figure S9, Supporting Information) suggest that the P(AA-MA)(5-1)–Fe–N and PAA–Fe–N catalysts have comparable peak intensity ratios of G-band (in-plane carbon)/D-band (carbon close to the edge), implying similar surface carbon species on the two catalysts.

To analyze the valence states of C and N on the catalyst surface, X-ray photoelectron spectroscopy (XPS) spectra were carried out. XPS survey spectra and elemental analyses are shown in Figure S10 and Table S1 (Supporting Information), respectively. As shown in **Figure 3**a, the high-resolution C 1s spectra of P(AA-MA)(5-1)–Fe–N and PAA–Fe–N catalysts can be nicely deconvoluted into three binding types at 284.7, 285.2, 286.9, and 288.8 eV, which corresponds to C−C, C−N, C−O, and π−π* bonds,[20] respectively (Table S2, Supporting Information). The formation of C−N bonds in two catalysts undoubtedly confirm that N has been successfully doped in the carbon network.[3c] In addition, the peak position of C−N bond in the P(AA-MA) (5-1)–Fe–N catalyst shows a positive shift compared to that of PAA–Fe–N (285.2 eV vs 285.0 eV), indicating a stronger interaction between Fe and N.[20]

Two peaks at ≈401.1 and 398.6 eV are observed in the high-resolution N 1s XPS spectra of the studied samples, which can be assigned to graphitic and pyridinic N species,[4c] respectively (Figure 3b). It is worth noting that P(AA-MA)(5-1)–Fe–N exhibits significantly higher surface N content (8.99 at%) as well as a higher pyridinic N/graphitic N ratio than that of PAA–Fe–N (1.83 at%). The surface Fe content of P(AA-MA)(5-1)–Fe–N is ≈3.5 times higher than that of PAA–Fe–N (0.44 vs 0.13 at%), and the Fe

content in bulk catalysts analyzed by inductively coupled plasma-mass spectrometry reveals a similar trend (ICP-MS, Table S3: Supporting Information). Therefore, it is speculated that it is likely that a high density of Fe–N_x/C active sites forms in the P(AA-MA)(5-1)-Fe–N catalyst after the introduction of MA.[3c,4c]

To provide further insights into the Fe–N structures existing in the studied samples, ^{57}Fe Mössbauer spectroscopy measurements were conducted (Figure 3c). The Mössbauer spectrum of the P(AA-MA)(5-1)–Fe–N catalyst consists of two doublets, which can be assigned to the high-spin Fe^{III}-N_4 (D1) and Fe^{II}-N_4 (D2) phases, respectively.[21] Apart from the D1 and D2 sites, one more doublet (D3) with high values of central shift (CS) and quadrupole splitting (QS) appears in the PAA–Fe–N sample (Table S4, Supporting Information). The CS value of 1.1 ± 0.1 mm s⁻¹ indicates that it stems from high spin ferrous ions (D2 site), but with a different Fe–N coordination structure from that in D2 due to the discrepancy of QS value. It is well known that electric quadrupole splitting is related to the electric field gradient (EFG) at the nucleus,[22] and the electric charges of neighboring ions or ligands distributed around a Mössbauer nucleus can contribute to the EFG tensor but only when they have a symmetry lower than cubic. The dominant component of the EFG tensor (V_{zz}) is inversely proportional to r^3: $(V_{zz})_{Lat} = \sum_i q_i \dfrac{3\cos^2\theta_i - 1}{r_i^3}$, where r indicates the distance between the Mössbauer nucleus and the neighboring ions. For the Fe ions with similar valence and spin states in the Fe–N–C catalysts, the QS values are primarily dependent on the Fe–N coordination structure. Hence, the D3 site (≈15%) with the considerable QS value reveals the existence of shorter Fe−N bonds in PAA–Fe–N compared to P(AA-MA)(5-1)–Fe–N.
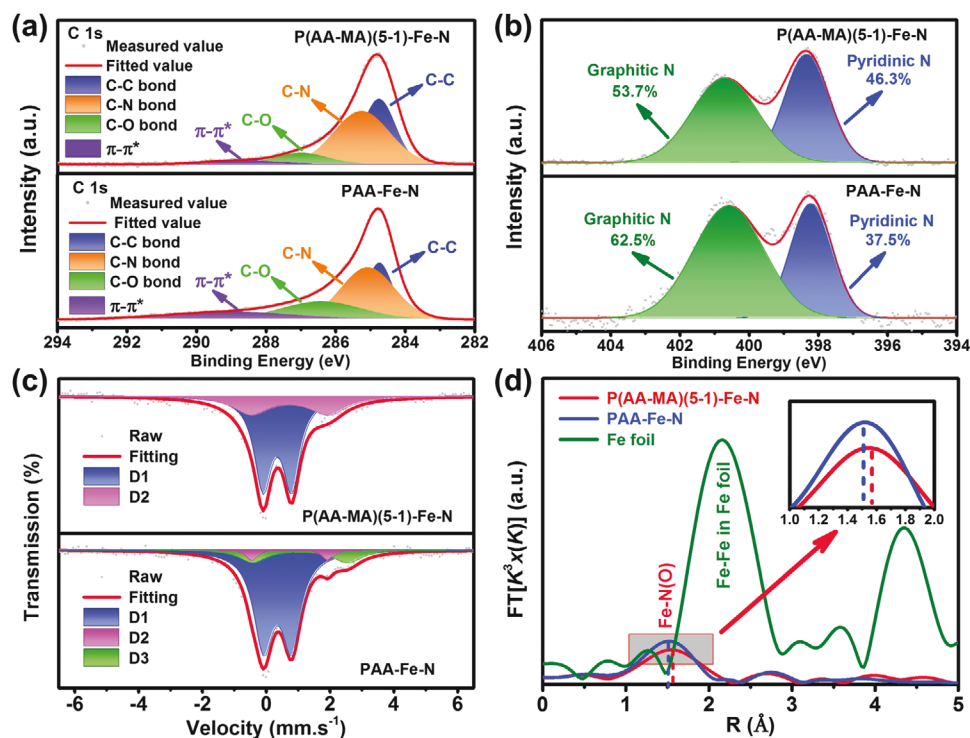

Figure 3. a,b) High-resolution C 1s (a) and N 1s (b) XPS spectra, and c) room-temperature ^{57}Fe Mössbauer spectra of the P(AA-MA)(5-1)–Fe–N and PAA–Fe–N samples. d) k^3-weighted FT-EXAFS spectra of P(AA-MA)(5-1)–Fe–N, PAA–Fe–N, and Fe foil samples.

**ADVANCED
SCIENCE NEWS**
www.advancedsciencenews.com

**ADVANCED
MATERIALS**
www.advmat.de

X-ray absorption spectroscopy (XAS) was carried out to detect the local Fe–N coordination structures of the studied samples. The Fe K-edge of the X-ray near-edge structures (XANES) of P(AA-MA)(5-1)–Fe–N and PAA–Fe–N were measured. As shown in Figure S11 (Supporting Information), the absorption edges of the XANES of Fe in the two catalysts are slightly negatively shifted relative to the Fe_2O_3 reference, implying that the oxidation state of Fe is between +2 and +3. The k^3-weighted Fourier transforms of the Fe K-edge extended X-ray absorption fine structure (FT-EXAFS) spectra of the catalysts were further analyzed (Figure 3d and Figures S12 and S13: Supporting Information) and the corresponding fitting parameters were listed in Table S5 (Supporting Information). Both P(AA-MA)(5-1)–Fe–N and PAA–Fe–N samples exhibit a prominent peak at ≈1.5 Å, mainly attributed to the Fe–N(O) first coordination shell.[21] Importantly, no apparent peaks at 2.2 Å corresponding to Fe-Fe pairs can be detected, in agreement with the ^{57}Fe Mössbauer spectroscopy and HAADF-STEM results. It demonstrates that Fe in both P(AA-MA)(5-1)–Fe–N and PAA–Fe–N catalysts can achieve atomic-level dispersion, and the single Fe atoms are coordinated with N(O) elements instead of being present as Fe—Fe bonds. It is worth noting that the peak position of the Fe–N(O) bond in PAA–Fe–N shifts slightly negative compared to that of P(AA-MA)(5-1)–Fe–N. The average bond lengths of Fe—N(O) in P(AA-MA)(5-1)–Fe–N and PAA–Fe–N catalysts are measured to be 2.035 and 2.006 Å, respectively. This result is consistent with that of ^{57}Fe Mössbauer spectroscopy, which shows that the mean Fe—N(O) bond length of PAA–Fe–N is shorter than in P(AA-MA)(5-1)–Fe–N. Based on the previous literature,[23] it is likely that some Fe–N_2 or Fe–N_3 species exist in the PAA–Fe–N sample (even though the fitted coordination number of Fe–N is still close to 4), leading to the decreased Fe–N(O) bond length. In contrast, the coordination structure of Fe–N sites in P(AA-MA)(5-1)–Fe–N should be Fe–N_4 dominant.

The electrocatalytic activity and stability of the developed catalysts were first evaluated by rotating ring-disk electrode (RRDE) in 0.5 м H_2SO_4 solution at 25 °C (**Figure 4**a). The cyclic voltammetry (CV) curves of the P(AA-MA)(5-1)–Fe–N and PAA–Fe–N catalysts in N_2 and O_2-saturated electrolytes were recorded, revealing a remarkable current response upon bubbling O_2 (Figure S14, Supporting Information). The half-wave potential ($E_{1/2}$) of the PAA–Fe–N catalyst is 0.822 V versus RHE, which is a respectable value for non-PGM ORR catalysts in acid. After the introduction of MA, all of the P(AA-MA)–Fe–N and MA–Fe–N catalysts demonstrate significantly enhanced ORR activity (Figure S15, Supporting Information). Specifically, the P(AA-MA)(5-1)–Fe–N catalyst reveals an optimal $E_{1/2}$ of 0.843 V, outperforming that of P(AA-MA)(3-1)–Fe–N (0.834 V), P(AA-MA)(1-1)–Fe–N (0.836 V), and MA–Fe–N (0.824 V). The measured ORR activity of P(AA-MA)(5-1)–Fe–N is comparable to that of Pt/C ($E_{1/2}$ ≈0.841 V) and is one of the best among reported ORR catalysts to date.[1b,4c,19,24] Additionally, P(AA-MA)(5-1)–Fe–N exhibits excellent selectivity with an extralow H_2O_2 yield (<1.2%) and electron transfer numbers (n) of ≈3.98 over the potential range from 0.2 to 0.8 V, signaling a complete reduction of O_2 to H_2O in a four-electron process. (Figure S16, Supporting Information). Also, P(AA-MA)(5-1)–Fe–N and PAA–Fe–N possess the close Tafel slopes, indicating that the rate-determining step of the ORR for these catalysts should be

the migration of adsorbed oxygenated species (Figure S17, Supporting Information).

The stability of the developed catalysts in half-cell conditions was then systematically evaluated. Interestingly, at 25 °C, both P(AA-MA)(5-1)–Fe–N and PAA–Fe–N catalysts exhibit superb stability in an accelerated stability tests (AST), with only 3 and 5 mV decay of $E_{1/2}$ after 5000 potential cycles between 0.6 and 1.0 V in O_2-saturated 0.5 м H_2SO_4, respectively. In order to evaluate the stability of the catalyst in practical PEMFC operation conditions, stability tests at elevated temperature, i.e., 60 °C, were performed (Figure 4b). Notably, the $E_{1/2}$ and limiting current density of the PAA–Fe–N catalyst degrade significantly after 5000 potential cycles at 60 °C, specifically by about 60 mV and 1.0 mA cm^{-2}, respectively. It suggests the performance degradation of PAA–Fe–N is substantially accelerated at 60 °C, pointing to a much more rapid damaging kinetics of Fe–N_x/C active sites at elevated temperatures. Importantly, the catalyst stability can be greatly improved in the presence of MA (Figure 4b and Figure S15: Supporting Information). After 5000 potential cycles at 60 °C, the P(AA-MA)(5-1)–Fe–N catalyst demonstrates extraordinarily high stability relative to all other the studied catalysts, with a negligible loss in $E_{1/2}$ (≈6 mV) and limiting current density. It suggests that the P(AA-MA)(5-1)–Fe–N catalyst with dominant Fe–N_4/C moieties and longer Fe—N bonds could maintain its structural integrity in the conditions similar to those in a PEMFC. This stability of the developed P(AA-MA)(5-1)–Fe–N catalyst, measured by RRDE in the acidic electrolyte, is among the highest when compared with previous works in the literature, considering that most of the reported catalysts are evaluated at ambient conditions (Figure 4c).[25]

In order to verify the versatility of the developed strategy in enhancing the stability of the M–N–C catalysts derived from other metals, we synthesized Co- and Mn-based PAA–M–N and P(AA-MA)–M–N catalysts using a similar synthesis process (Figure S18, Supporting Information). As shown in Figure 4d and Figure S19 (Supporting Information), it is noticeable that P(AA-MA)–Co(or Mn)–N catalysts also exhibit superior electrochemical performance to their PAA counterparts after 5000-cycle AST. This result demonstrates that our method is an effective and universal strategy for improving the stability of M–N–C ORR catalysts.

The detailed mechanisms of catalyst performance degradation at 60 °C in half-cells are investigated by physical and structural characterizations. XRD patterns and TEM images of the catalysts after AST tests reveal similar diffraction peaks and sheet-like structures to the initial ones, respectively (Figures S20 and S21: Supporting Information). The corresponding FT-EXAFS spectra of the two catalysts are shown in Figure 4e,f, respectively (Figures S22 and S23, Supporting Information). For the P(AA-MA)(5-1)–Fe–N catalyst, there is no significant Fe—Fe bond formation after AST, demonstrating the robustness of Fe–N bonds, and subsequently, the catalyst's high tolerance to Fe demetalation. In contrast, the peak at 2.7 Å attributable to Fe—Fe bond in the Fe_2O_3 sample increases sharply for the PAA–Fe–N catalyst after 5000 cycles compared to the initial one. This result unambiguously determines that the demetalation of Fe–N_x/C sites does take place in the PAA–Fe–N catalyst during the stability test at 60 °C and that a part of the detached Fe atoms likely migrate and form trace amounts of Fe_2O_3 clusters
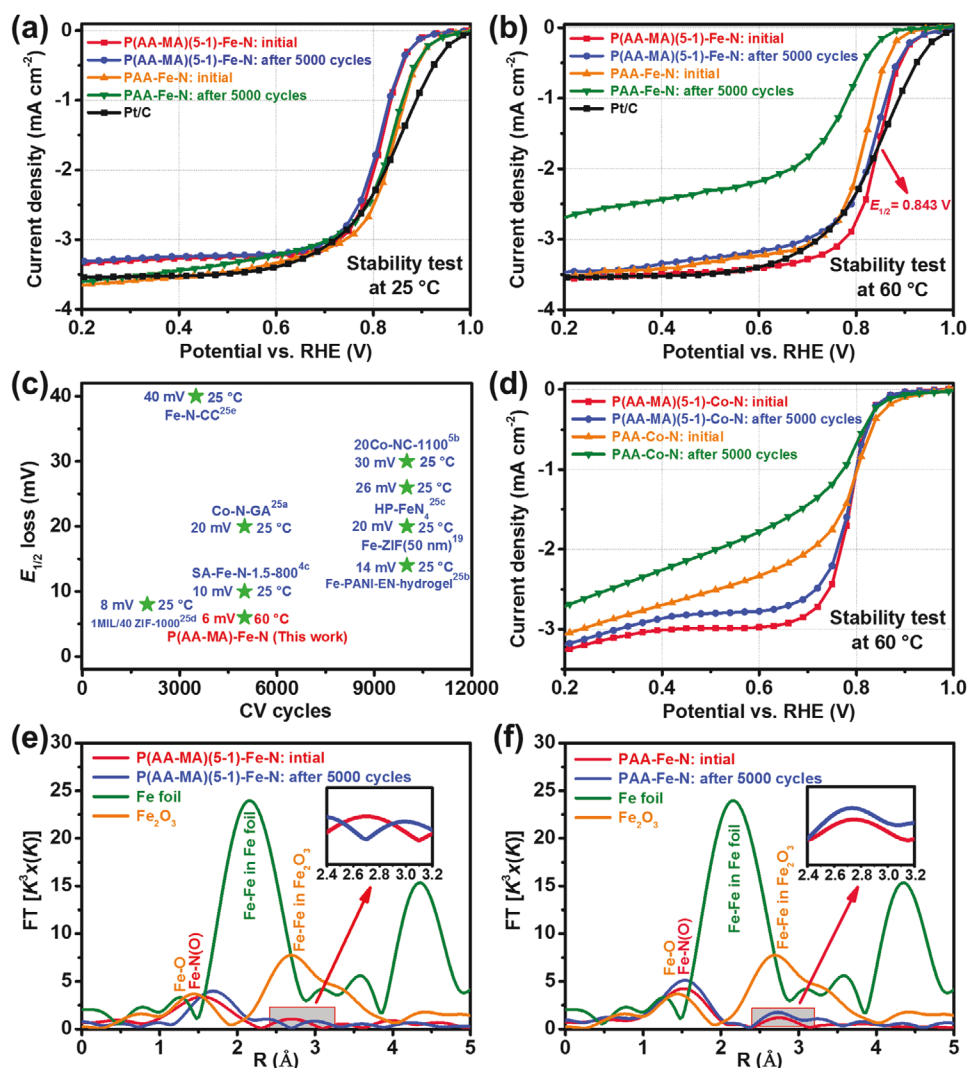
**ADVANCED
SCIENCE NEWS**

www.advancedsciencenews.com

**ADVANCED
MATERIALS**

www.advmat.de

Figure 4. a,b) ORR polarization curves of P(AA-MA)(5-1)–Fe–N and PAA–Fe–N catalysts before and after 5000-cycle AST in an O_2-saturated 0.5 M H_2SO_4 solution at 25 °C (a) and 60 °C (b), catalyst loading: 0.6 $mg_{non-PGM}$ cm^{-2}, disk rotation rate: 900 rpm. c) $E_{1/2}$ losses of previously reported M–N–C catalysts after different cycling numbers of AST from 0.6–1.0 V in O_2-saturated 0.5 M H_2SO_4. d) The ORR polarization curves of P(AA-MA)–Co–N and PAA–Co–N catalysts before and after AST. e,f) k^3-weighted FT-EXAFS spectra of P(AA-MA)(5-1)–Fe–N, PAA–Fe–N (before and after AST), Fe foil, and Fe_2O_3 samples.

which cannot be identified in XRD. Elemental analyses by XPS (Table S1, Supporting Information) demonstrates that after AST, the Fe content of PAA–Fe–N rises remarkably from 0.13 to 8.48% while P(AA-MA)(5-1)–Fe–N exhibits significantly less surface Fe aggregation (0.44 to 2.89 at%). Even worse, the destroyed Fe–N$_x$/C structure would promote Fenton reactions[9a] and further accelerate the cleavage of adjacent Fe−N bonds, an outcome consistent with the electron energy loss spectroscopy (EELS) result reported previously.[3c] Note that other degradation mechanisms, such as carbon corrosion, may occur simultaneously on PAA–Fe–N as the C content is significantly decreased from 83.62% to 58.07% after AST (Table S1, Supporting Information).

The developed Fe–N–C catalysts were implemented in a PEMFCs cathode to evaluate their MEA performance. The polarization and power density plots for H_2–O_2/air fuel cells with benchmark Pt/C catalysts are presented in Figure S24

(Supporting Information). In good agreement with RDE data, P(AA-MA)(5-1)–Fe–N exhibits much enhanced open-cell voltage (OCV) (0.960 V vs 0.941 V) and current density over the entire voltage range compared to PAA–Fe–N. The current density at the kinetic region (0.8 V) and maximum power density of the P(AA-MA)(5-1)–Fe–N catalyst reach 0.21 A cm^{-2} and 0.65 W cm^{-2} (at 1266 mA cm^{-2}) (**Figure 5**a), respectively, which is on par with the state-of-the-art fuel cell performance based on non-PGM catalysts[3c,24,26] (Table S6, Supporting Information). Similarly, P(AA-MA)(5-1)–Fe–N exhibits excellent performance under H_2–air conditions, with the current density at 0.6 V (0.45 A cm^{-2}) higher than that of PAA–Fe–N (0.25 A cm^{-2}, Figure 5b). The stability of P(AA-MA)(5-1)–Fe–N and PAA–Fe–N were evaluated in H_2–air mode at a constant voltage of 0.55 V (Figure 5c and Figure S25: Supporting Information). In agreement with AST on RDE at 60 °C, the stability of the P(AA-MA)(5-1)–Fe–N catalyst at the fuel cell cathode is far better than that of PAA–Fe–N,
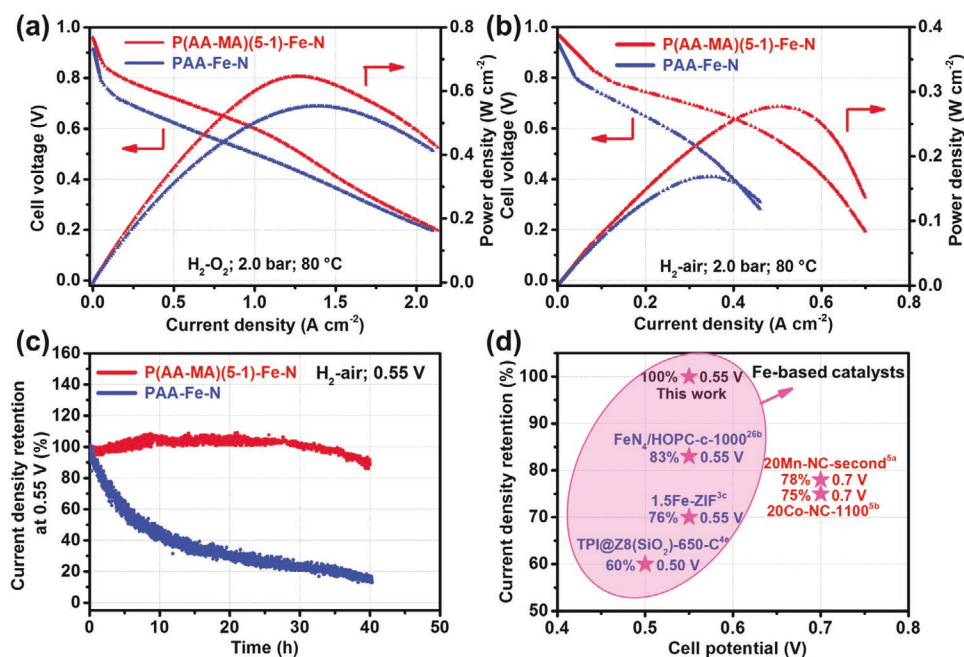
**ADVANCED
SCIENCE NEWS**

www.advancedsciencenews.com

**ADVANCED
MATERIALS**

www.advmat.de

Figure 5. a,b) Fuel cell performance of P(AA-MA)(5-1)–Fe–N and PAA–Fe–N catalysts under H_2–O_2 (a) and H_2–air (b) conditions, cathode loading: 3.0 mg cm^{-2}. c) Current density retention of P(AA-MA)(5-1)–Fe–N and PAA–Fe–N catalysts during stability tests at a constant voltage of 0.55 V in PEMFCs. d) Current density retention in the first 20 h of various M–N–C catalysts tested in H_2–air fuel cells.

with its retention rate of current density approaching 100% for the first 37 h. To the best of our knowledge, this outstanding stability performance in the first 20 h of durability test surpasses most reported catalysts (Figure 5d and Table S6: Supporting Information).[3c,4e,26b] Based on the stability performance measured on RDE and PEMFCs, we can surmise that we have indeed developed an effective strategy to improve the durability of the M–N–C catalysts and the structural integrity of M–N$_x$/C active sites by enhancing the binding constant between metal ions and chelating polymers and tuning the M—N bond length.

To further explore the origin of the great difference in stability of the P(AA-MA)(5-1)–Fe–N and PAA–Fe–N catalysts, density functional theory (DFT) calculations were performed to investigate the adsorption energy of the Fe atoms on the support (E_{ad}) and the difference between E_{ad} and the bulk cohesive energy (E_{coh}). In order to use DFT calculations here, the difference in bond length of the two catalysts is dependent on different Fe–N$_x$ coordination compositions (Based on the fitting results of Mössbauer spectroscopy, about 15% of Fe–N$_2$/N$_3$ species are present in the PAA–Fe–N catalyst), which are defined as:[27]

$$E_{ad} = E_{Fe-Nx/C} - E_{Nx/C} - E_{free-atom} \qquad (1)$$

$$E_{coh} = E_{bulk} - n \times E_{free-atom} \qquad (2)$$

where n is the number of Fe atoms in the bulk Fe. If $E_{ad} < 0$ and $E_{ad} - E_{coh} < 0$, then the Fe atoms embedded into the support are expected to be stable against either the metal leaching or aggregating. More negative values in E_{ad} and $E_{ad} - E_{coh}$ mean that the embedding of Fe atoms into the N–C matrix is more stable.

Figure 6a,b shows the calculated E_{ad} and $E_{ad} - E_{coh}$ values on the Fe–N$_2$/C, Fe–N$_3$/C, and Fe–N$_4$/C structures. All three

structures are stable against the metal being leached from the support due to the negative E_{ad} values. However, Fe–N$_2$/C and Fe–N$_3$/C possess positive E_{ad} – E_{coh} values, suggesting that they are less stable against metal clustering when compared with Fe–N$_4$/C. Although the inclusion of the solvation correction may stabilize Fe–N$_3$/C slightly, its calculated $E_{ad} - E_{coh}$ is still 0.27 eV above the zero lines. Among the three catalysts, Fe–N$_4$/C is the most stable against both metal leaching and clustering and is consistent with our experimental results.

In Figure 6c,d,e, we display the differential charge density of Fe anchored on the N$_2$/C, N$_3$/C, and N$_4$/C supports, respectively. The positive (negative) value of the differential charge density indicates charge accumulation (deficit) when Fe is adsorbed onto the support. Additionally, the Fe—N bonding strength is nearly the same within each Fe–N$_x$/C structure due to their symmetrical charge distributions. Interestingly, we find that the Fe—N bonding strength is also the same in different Fe–N$_x$/C structures. By performing Bader charge analyses, we find that there are charge transfers from the Fe atoms to coordinated N atoms on the three catalysts, which are calculated as 0.22, 0.29, and 0.25 e per N atom on Fe–N$_2$/C, Fe–N$_3$/C, and Fe–N$_4$/C, respectively. The approximately equal Fe–N charge transfer in different Fe–N$_x$/C structures renders Fe—N bonds with equal strength. As a result, the more coordinated N atoms around the anchored Fe atom on the support (such as that in Fe–N$_4$/C), the more stable the structure will be.

In summary, a general and effective strategy to improve the stability of M–N–C catalysts is developed by regulating the interaction between metal ions and polymers in the catalyst precursor, which allows for the fine-tuning of M—N bond length and coordination in the final catalysts. Compared to PAA–Fe–N with 15% low-coordinated Fe–N$_2$/N$_3$ moieties, the copolymerized P(AA-MA)(5-1)–Fe–N catalyst with exclusive Fe–N$_4$/C sites and
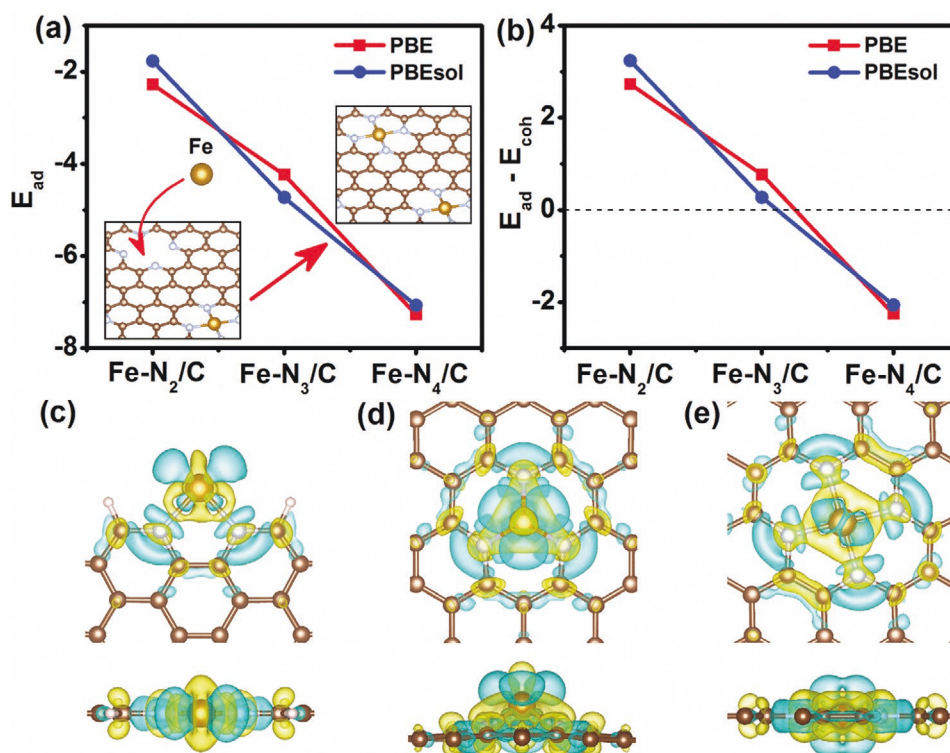
Figure 6. a) The adsorption energy (E_{ad}) and b) the difference between the adsorption energy and the cohesive energy (E_{coh}) of the Fe–N$_x$/C system calculated without (red) and with (blue) solvation correction. A more negative value means that the embedded Fe atoms in the support is more stable against metal leaching or clustering. The structure and differential charge density isosurfaces for c) Fe–N$_2$/C, d) Fe–N$_3$/C, and e) Fe–N$_4$/C, respectively. The cyan and yellow isosurfaces correspond to the charge density contour of -0.02 and $+0.02$ e Å. The big brown, gray, light gray, and small white spheres represent Fe, C, N, and H atoms, respectively.

longer Fe—N bonds is significantly better performing, an observation evidenced by ^{57}Fe Mössbauer spectroscopy and XAS. The best-performing P(AA-MA)(5-1)–Fe–N catalyst exhibits extraordinarily high activity and stability both in half-cell and H$_2$–air fuel cells, with an $E_{1/2}$ loss of only 6 mV after AST 60 °C and a nearly unchanged current density for 37 h at 0.55 V, respectively, among the best overall performance in its class reported so far. DFT calculations reveal that P(AA-MA)(5-1)–Fe–N possesses both a more negative adsorption energy of the Fe atoms (E_{ad}) as well as a more negative difference between E_{ad} and the bulk cohesive energy ($E_{ad} - E_{coh}$) than PAA–Fe–N, accounting for its outstanding structural stability and tolerance to demetalation. Solving water flooding, carbon corrosion, and other issues may further advance the applications of non-PGM cathodes in PEMFCs, ventures which are ongoing in our laboratory.

Supporting Information

Supporting Information is available from the Wiley Online Library or from the author.

Acknowledgements

Conflict of Interest

The authors declare no conflict of interest.

Data Availability Statement

The data that support the findings of this study are available from the corresponding author upon reasonable request.

Keywords

[1] a) M. H. Shao, Q. W. Chang, J. P. Dodelet, R. Chenitz, *Chem. Rev.* **2016**, *116*, 3594; b) G. Wu, K. L. More, C. M. Johnston, P. Zelenay, *Science* **2011**, *332*, 443.

[2] a) X. X. Wang, M. T. Swihart, G. Wu, *Nat. Catal.* **2019**, *2*, 578; b) Y. Dong, M. Zhou, W. Tu, E. Zhu, Y. Chen, Y. Zhao, S. Liao, Y. Huang, Q. Chen, Y. Li, *Adv. Funct. Mater.* **2019**, *29*, 1900015.

[3] a) Y. S. Zhao, J. W. Wan, H. Y. Yao, L. J. Zhang, K. F. Lin, L. Wang, N. L. Yang, D. B. Liu, L. Song, J. Zhu, L. Gu, L. Liu, H. J. Zhao, Y. L. Li, D. Wang, *Nat. Chem.* **2018**, *10*, 924; b) J. Liu, M. G. Jiao, L. L. Lu, H. M. Barkholtz, Y. P. Li, Y. Wang, L. H. Jiang, Z. J. Wu, D. J. Liu, L. Zhuang, C. Ma, J. Zeng, B. S. Zhang, D. S. Su, P. Song, W. Xing, W. L. Xu, Y. Wang, Z. Jiang, G. Q. Sun, *Nat. Commun.* **2017**, *8*, 15938; c) H. G. Zhang, H. T. Chung, D. A. Cullen, S. Wagner, U. I. Kramm, K. L. More, P. Zelenay, G. Wu, *Energy Environ. Sci.* **2019**, *12*, 2548; d) P. Du, Y. Bao, C. Guo, L. Wu, J. Pan, C. Zhao, F.-X. Ma, J. Lu, Y. Y. Li, *Chem. Commun.* **2020**, *56*, 14467; e) C. Chen, Y. Dong, J. Ma, L. Zheng, Y. Zhao, W. Chen, Y. Li, *Mater. Chem. Front.* **2021**, *5*, 2684.

[4] a) Q. Li, R. Cao, J. Cho, G. Wu, *Adv. Energy Mater.* **2014**, *4*, 1301415; b) Y. Zheng, Y. Jiao, Y. H. Zhu, Q. R. Cai, A. Vasileff, L. H. Li, Y. Han, Y. Chen, S. Z. Qiao, *J. Am. Chem. Soc.* **2017**, *139*, 3336; c) Z. P. Miao, X. M. Wang, M. C. Tsai, Q. Q. Jin, J. S. Liang, F. Ma, T. Y. Wang, S. J. Zheng, B. J. Hwang, Y. H. Huang, S. J. Guo, Q. Li, *Adv. Energy Mater.* **2018**, *8*, 1801226; d) A. Zitolo, V. Goellner, V. Armel, M. T. Sougrati, T. Mineva, L. Stievano, E. Fonda, F. Jaouen, *Nat. Mater.* **2015**, *14*, 937; e) X. Wan, X. F. Liu, Y. C. Li, R. H. Yu, L. R. Zheng, W. S. Yan, H. Wang, M. Xu, J. L. Shui, *Nat. Catal.* **2019**, *2*, 259; f) Y. Du, F.-X. Ma, C.-Y. Xu, J. Yu, D. Li, Y. Feng, L. Zhen, *Nano Energy* **2019**, *61*, 533.

[5] a) J. Z. Li, M. J. Chen, D. A. Cullen, S. Hwang, M. Y. Wang, B. Y. Li, K. X. Liu, S. Karakalos, M. Lucero, H. G. Zhang, C. Lei, H. Xu, G. E. Sterbinsky, Z. X. Feng, D. Su, K. L. More, G. F. Wang, Z. B. Wang, G. Wu, *Nat. Catal.* **2018**, *1*, 935; b) X. X. Wang, D. A. Cullen, Y. T. Pan, S. Hwang, M. Y. Wang, Z. X. Feng, J. Y. Wang, M. H. Engelhard, H. G. Zhang, Y. H. He, Y. Y. Shao, D. Su, K. L. More, J. S. Spendelow, G. Wu, *Adv. Mater.* **2018**, *30*, 1706758.

[6] W. Wang, Q. Y. Jia, S. Mukerjee, S. L. Chen, *ACS Catal.* **2019**, *9*, 10126.

[7] a) J. Y. Choi, L. J. Yang, T. Kishimoto, X. G. Fu, S. Y. Ye, Z. W. Chen, D. Banham, *Energy Environ. Sci.* **2017**, *10*, 296; b) Y. Y. Shao, J. P. Dodelet, G. Wu, P. Zelenay, *Adv. Mater.* **2019**, *31*, 1807615.

[8] a) C. H. Choi, C. Baldizzone, G. Polymeros, E. Pizzutilo, O. Kasian, A. K. Schuppert, N. R. Sahraie, M. T. Sougrati, K. J. J. Mayrhofer, F. Jaouen, *ACS Catal.* **2016**, *6*, 3136; b) K. Kumar, P. Gairola, M. Lions, N. Ranjbar-Sahraie, M. Mermoux, L. Dubau, A. Zitolo, F. Jaouen, F. Maillard, *ACS Catal.* **2018**, *8*, 11264; c) R. Chenitz, U. I. Kramm, M. Lefevre, V. Glibin, G. X. Zhang, S. H. Sun, J. P. Dodelet, *Energy Environ. Sci.* **2018**, *11*, 365; d) M. Ferrandon, X. P. Wang, A. J. Kropf, D. J. Myers, G. Wu, C. M. Johnston, P. Zelenay, *Electrochim. Acta* **2013**, *110*, 282; e) K. Mamtani, D. Singh, J. Tian, J. M. M. Millet, J. T. Miller, A. C. Co, U. S. Ozkan, *Catal. Lett.* **2016**, *146*, 1749.

[9] a) K. Kumar, L. Dubau, M. Mermoux, J. Li, A. Zitolo, J. Nelayah, F. Jaouen, F. Maillard, *Angew. Chem., Int. Ed.* **2020**, *59*, 3235; b) H. Schulenburg, S. Stankov, V. Schunemann, J. Radnik, I. Dorbandt, S. Fiechter, P. Bogdanoff, H. Tributsch, *J. Phys. Chem. B* **2003**, *107*, 9034; c) U. I. Kramm, M. Lefevre, P. Bogdanoff, D. Schmeisser, J. P. Dodelet, *J. Phys. Chem. Lett.* **2014**, *5*, 3750; d) V. Goellner, C. Baldizzone, A. Schuppert, M. T. Sougrati, K. Mayrhofer, F. Jaouen, *Phys. Chem. Chem. Phys.* **2014**, *16*, 18454;

e) C. H. Choi, C. Baldizzone, J. P. Grote, A. K. Schuppert, F. Jaouen, K. J. J. Mayrhofer, *Angew. Chem., Int. Ed.* **2015**, *54*, 12753.

[10] a) G. X. Zhang, R. Chenitz, M. Lefevre, S. Sun, J. P. Dodelet, *Nano Energy* **2016**, *29*, 111; b) L. J. Yang, N. Larouche, R. Chenitz, G. X. Zhang, M. Lefevre, J. P. Dodelet, *Electrochim. Acta* **2015**, *159*, 184.

[11] a) J. Herranz, F. Jaouen, M. Lefevre, U. I. Kramm, E. Proietti, J. P. Dodelet, P. Bogdanoff, S. Fiechter, I. Abs-Wurmbach, P. Bertrand, T. M. Arruda, S. Mukerjee, *J. Phys. Chem. C* **2011**, *115*, 16087; b) G. Liu, X. G. Li, J. W. Lee, B. N. Popov, *Catal. Sci. Technol.* **2011**, *1*, 207.

[12] X. Xie, C. He, B. Li, Y. He, D. A. Cullen, E. C. Wegener, A. J. Kropf, U. Martinez, Y. Cheng, M. H. Engelhard, *Nat. Catal.* **2020**, *3*, 1044.

[13] P. Du, X. Xiao, F. Ma, H. Wang, J. Shen, F. Lyu, Y. Chen, J. Lu, Y. Li, *ACS Appl. Nano Mater.* **2020**, *3*, 5637.

[14] a) B. L. Rivas, E. D. Pereira, I. Moreno-Villoslada, *Prog. Polym. Sci.* **2003**, *28*, 173; b) P. Souda, L. Sreejith, *Polym. Bull.* **2014**, *71*, 839.

[15] a) Y. R. Qiu, L. J. Mao, *Desalination* **2013**, *329*, 78; b) M. Dandapat, D. Mandal, *Phys. Chem. Chem. Phys.* **2016**, *18*, 2564.

[16] B. C. Trivedi, B. M. Culbertson, *MaleicAnhydride*, Plenum Press, New York, USA **1982**.

[17] a) C. A. Brautigam, H. Y. Zhao, C. Vargas, S. Keller, P. Schuck, *Nat. Protoc.* **2016**, *11*, 882; b) B. Sharma, S. Striegler, M. Whaley, *ACS Catal.* **2018**, *8*, 7710.

[18] a) G. Camci-Unal, N. L. B. Pohl, *J. Chem. Eng. Data* **2010**, *55*, 1117; b) J. L. Xu, L. K. Koopal, L. C. Fang, J. Xiong, W. F. Tan, *Environ. Sci. Technol.* **2018**, *52*, 4099.

[19] H. G. Zhang, S. Hwang, M. Y. Wang, Z. X. Feng, S. Karakalos, L. L. Luo, Z. Qiao, X. H. Xie, C. M. Wang, D. Su, Y. Y. Shao, G. Wu, *J. Am. Chem. Soc.* **2017**, *139*, 14143.

[20] C. Tang, B. Wang, H. F. Wang, Q. Zhang, *Adv. Mater.* **2017**, *29*, 1703185.

[21] W. G. Liu, L. L. Zhang, X. Liu, X. Y. Liu, X. F. Yang, S. Miao, W. T. Wang, A. Q. Wang, T. Zhang, *J. Am. Chem. Soc.* **2017**, *139*, 10790.

[22] Y. L. Chen, D. P. Yang, *Mössbauer Effect in Lattice Dynamics*, Wiley-VCH, Weinheim **2007**.

[23] a) H. J. Shen, E. Gracia-Espino, J. Y. Ma, H. D. Tang, X. Mamat, T. Wagberg, G. Z. Hu, S. J. Guo, *Nano Energy* **2017**, *35*, 9; b) C. Z. Zhu, Q. R. Shi, B. Z. Xu, S. F. Fu, G. Wan, C. Yang, S. Y. Yao, J. H. Song, H. Zhou, D. Du, S. P. Beckman, D. Su, Y. H. Lin, *Adv. Energy Mater.* **2018**, *8*, 1801956.

[24] X. G. Fu, N. Li, B. H. Ren, G. P. Jiang, Y. R. Liu, F. M. Hassan, D. Su, J. B. Zhu, L. Yang, Z. Y. Bai, Z. P. Cano, A. P. Yu, Z. W. Chen, *Adv. Energy Mater.* **2019**, *9*, 1803737.

[25] a) X. Fu, J. Y. Choi, P. Zamani, G. Jiang, M. A. Hoque, F. M. Hassan, Z. Chen, *ACS Appl. Mater. Interfaces* **2016**, *8*, 6488; b) Z. Qiao, H. Zhang, S. Karakalos, S. Hwang, J. Xue, M. Chen, D. Su, G. Wu, *Appl. Catal., B* **2017**, *219*, 629; c) N. Zhang, T. Zhou, M. Chen, H. Feng, R. Yuan, C. a. Zhong, W. Yan, Y. Tian, X. Wu, W. Chu, C. Wu, Y. Xie, *Energy Environ. Sci.* **2020**, *13*, 111; d) H. Wang, F. X. Yin, N. Liu, R. H. Kou, X. B. He, C. J. Sun, B. H. Chen, D. J. Liu, H. Q. Yin, *Adv. Funct. Mater.* **2019**, *29*, 1901531; e) G. A. Ferrero, K. Preuss, A. Marinovic, A. B. Jorge, N. Mansor, D. J. Brett, A. B. Fuertes, M. Sevilla, M. M. Titirici, *ACS Nano* **2016**, *10*, 5922.

[26] a) Y. J. Deng, B. Chi, J. Li, G. H. Wang, L. Zheng, X. D. Shi, Z. M. Cui, L. Du, S. J. Liao, K. T. Zang, J. Luo, Y. F. Hu, X. L. Sun, *Adv. Energy Mater.* **2019**, *9*, 1802856; b) M. Qiao, Y. Wang, Q. Wang, G. Hu, X. Mamat, S. Zhang, S. Wang, *Angew. Chem., Int. Ed.* **2020**, *59*, 2688.

[27] H. X. Xu, D. J. Cheng, D. P. Cao, X. C. Zeng, *Nat. Catal.* **2018**, *1*, 339.